



Fault Detection and Location in Power Systems with Large-Scale Photovoltaic Power Plant by Adaptive Distance Relays

A. Jodaei, Z. Moravej*

Faculty of Electrical & Computer Engineering, Semnan University, Semnan, Iran

P A P E R I N F O

Paper history:

Received 15 October 2023

Accepted in revised form 28 November 2023

Keywords:

Apparent impedance
Distance relay
Fault detection
Fault location
Large scale photovoltaic power plant
Transmission line

A B S T R A C T

In this paper, a novel approach is introduced for Fault Detection and Fault Location in power systems that incorporate Large-Scale Photovoltaic Power Plants (LSPPPs). Given that short-circuit (SC) characteristics in photovoltaic systems differ significantly from those observed in traditional Synchronous Generators (SGs). The increasing integration of LSPPPs into the power grid is anticipated to have an impact on the performance of conventional protection relay systems; initially designed for SG-dominated setups. Therefore, the proposed method revolves around analyzing the influence of LSPPPs on the alteration of observed transmission line impedance to identify and locate faults accurately. Furthermore, the methodology takes into consideration factors such as fault location, fault resistance, fault type, changing the LSPPP generation, and noise conditions. when calculating the phase angle of the fault loop current. The effectiveness of this approach was assessed through testing and evaluation on 2-bus and IEEE 39-bus test systems connected to an LSPPP, simulated using PSCAD/EMTDC and MATLAB/SIMULINK.

Doi: 10.5829/ijee.2024.15.03.05

NOMENCLATURE

| | | | |
|------------|---|-------------|---|
| RES | Renewable energy systems | E_M | Internal voltage of LSPPP |
| PV | Photovoltaic systems | Z_M | impedance of LSPPP |
| LSPPP | Large-scale photovoltaic power plant | R_{app} | Resistance of Z_{app} |
| SG | Synchronous generators | X_{app} | Reactance of Z_{app} |
| Z_L | Impedance of the MN line | α | Phase angles of V_{rM} |
| R_f | Fault resistance | β | Phase angle of I_{rM} |
| I_f | Fault loop current | γ | Faulted path current phase |
| Z_{app} | Apparent impedance calculated by relay | ΔZ | Correction impedance |
| V_{rM} | Operating voltage at bus M | K_{oL} | Zero-sequence compensation |
| I_{rM} | Operating current at bus M | φ | Deviation angle |
| x | Per unit fault distance | (d, q) | Axis component |
| θ_L | Line impedance angle | $(1, 2, 0)$ | Positive Sequence, negative sequence, zero components |
| Z_{MF} | Impedance between bus M and fault point | f | Superscript indicates the measurements during fault |
| E_N | Equivalent internal voltage of grid | PCC | Point of common coupling |
| Z_N | Equivalent impedance of grid | R_{ph} | Arcing resistance |

*Corresponding Author Email: zmoravej@semnan.ac.ir (Z. Moravej)

Please cite this article as: Jodaei A, Moravej Z. Fault Detection and Location in Power Systems with Large-Scale Photovoltaic Power Plant by Adaptive Distance Relays, Iranica Journal of Energy and Environment, 2024 July, 15(3): 265-78. Doi: 10.5829/ijee.2024.15.03.05

INTRODUCTION

The considerable decrease in the cost of PV systems in recent years has spurred a rapid and extensive deployment of these systems worldwide. Specifically, LSPPPs now make up approximately 66% of all solar power plants in operation. This proliferation carries significant implications for the electrical power infrastructure (1, 2). Power plants of this nature must comply with specific grid codes (GCs) to enhance network integration and system stability. The increasing integration of LSPPP into the power system has raised concerns among researchers due to its potential impact on network stability. When utilizing renewable power plants, it is crucial to consider the requirements outlined in modern GCs (3-5). The introduction of new GCs broadens the scope of network services. Ryu et al. (6) addressed the discussions center around Fast Frequency Response, Power Oscillation Damping, and Hasanien (7) pointed out the control of power fluctuations. Furthermore, Haddadi et al. (8) aimed to enhance Fault Ride-Through (FRT) capabilities. Electronic power converters, which are used to connect solar power plants to the power grids (9). The primary distinction between PV and SG lies in the presence of power converters (10). This distinction necessitates researchers to modify the conventional SC current calculation method (11-13). SG-generated fault currents exhibit high amplitude and uncontrolled characteristics. Various factors, such as the source electrical parameters and SC impedance, influence these currents. Conversely, PV-generated fault currents possess low amplitude and are influenced by the control scheme of switching power electronic devices. In traditional systems, relays are typically adjusted based on the high-amplitude SC currents and inductive effects resulting from SGs. Certainly, as the integration of PV systems grows and fault current characteristics evolve, the likelihood of the protection system malfunctioning also increases. The effectiveness of protection systems has been a subject of discussion in various sources. For instance, literature (14-18) delve into the topic of distance protection; while, Kou et al. (19-21) putted forward protection methods centered n negative sequence components. In addition, Haddadi et al. and Singh et al.(22, 23) introduced a communication-assisted approach for fault identification. Finally, Rosini et al. (24) built upon principles related to frequency change rate and power swing protection. In power systems where power converters are integrated, there is a necessity to devise a novel control system with a different architecture in contrast to traditional systems. This becomes pivotal due to the potential implications of converter additions on system stability (25, 26). The LSPPP can be managed through either a centralized or decentralized structure, as discussed by Al Awadhi and El Moursi (26-28). Typically, LSPPP systems employ a Power Plant Central Controller (PPC) for control and coordination. In scenarios where LSPPP is integrated

with the transmission network, a centralized frequency control approach is implemented, as highlighted by Ryu et al. (6, 26). However, when LSPPP is connected to microgrids or distribution networks, a decentralized strategy, as elaborated by Al Awadhi and El Moursi (26). Nevertheless, voltage control at the LSPPP connection point to the grid follows a centralized structure in compliance with GC requirements (29). The deployment of LSPPP within the network imposes limitations on the magnitude of fault currents and induces alterations in their phase angles. These changes in fault characteristics directly impinge upon the operational performance of distance relays, and this effect becomes more pronounced with higher fault resistance values (30). To mitigate the impact of fault resistance, a novel solution, referred to as the adaptive distance relay method, presented by Gallo et al. (31).

The variability of solar radiation introduces yet another crucial element that heightens the potential for instability within the PCC of the system. Furthermore, the diminishing inertia in the system, resulting from the absence of rotating machinery found in traditional power plants, can contribute to network instability. In response to these challenges, it becomes imperative to scrutinize GCs to ensure the reliable integration of PV systems in LSPPPs. This need arises from the necessity for new GCs tailored to the specific requirements of these LSPPPs, enhancing both their configuration and control stability (32). Additional complications, such as voltage drops and grid losses in systems with high LSPPP penetration, are thoroughly examined by Paladhi and Pradhan (33). The presence of renewable power sources like LSPPP within the network induces alterations in the impedance path as perceived by distance relays, diverging from the impedance path associated with traditional generation sources, a phenomenon comprehensively elaborated by Rajapakse et al. (34).

This study presents an innovative approach to enhance the robustness of distance protection systems along with a fault location algorithm for transmission lines in the presence of LSPPP. The primary aim is to minimize the interference caused by converter interfaces on impedance measurements, thus ensuring the reliable operation of the protection system. The proposed method leverages the phase angle of the fault loop to estimate apparent impedance variations attributable to LSPPP. A comprehensive evaluation of this approach has been conducted through simulations on a 2-bus and IEEE 39-bus test systems connected to LSPPP using the PSCAD/EMTDC software. Then the required signals are taken from PSCAD/EMTDC platform and MATLAB software is used to signal processing and extract the required angles. Various scenarios have been explored, including different fault types, fault locations, fault resistances, and LSPPP generation levels, to assess their impact on the performance of the distance protection system and the effectiveness of the proposed mitigation

technique. In this article, the Euclidean distance index is used to benchmark the proposed method and this index is compared for the proposed method with the traditional method in systems with SG and systems with LSPPP. This algorithm, in addition to its excellent fault detection capability, also possesses the ability to the fault location. The performance of the proposed method has been investigated with a sample frequency of 2 kHz, which is reduced compared to other articles, which reduces the volume of calculations and increases the speed of fault detection and fault location.

Effect of LSPPP on fault current

As highlighted in the preceding section, it's noteworthy that the SC fault current in a network connected to LSPPP diverges from that in traditional networks. One of the paramount factors contributing to this discrepancy is the control scheme implemented in electronic power devices. These control strategies are contingent upon the requisites of the GC, and they must be designed to prevent the occurrence of thermal stress in electronic power switches. To observe these variances, Figure 1 is subjected to simulation, and its outcomes are subsequently juxtaposed with those of a conventional system. It is worth noting that a solar power plant can be effectively modeled as an equivalent voltage source (E_M) in conjunction with an equivalent impedance in series (Z_M) (35). Detailed specifications of the simulated system are expounded upon in the section “Simulation results”.

In a broader context, the characteristics of SC currents in the presence of LSPPP can be summarized as follows:

- Amplitude of fault current: The magnitude of fault current in networks connected to LSPPP is contingent upon the inverter terminal voltage value (36) The converter incorporates a current limiter mechanism, and the fault current range is regulated by the control scheme. This value closely approximates the nominal load current, ensuring the protection of electronic power devices. Figure 2 provides a comparative analysis of fault currents between SG and LSPPP for a specific unbalanced fault.

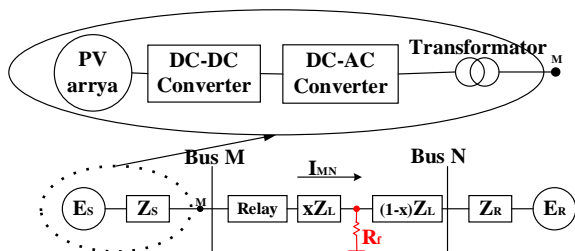


Figure 1. Transmission network in the presence of LSPPP

- Positive, negative, and zero current sequences: In networks connected to LSPPP, the negative sequence component value is typically reduced or entirely eliminated, depending on the inverter control strategy and the requisites of the network code in use. Additionally, these systems often entirely eliminate the zero-sequence component (10). Figure 3 illustrates the comparative analysis of zero, negative, and positive fault sequence magnitudes between SG and LSPPP.
- Phase angle: In networks connected to LSPPP, the phase angle of fault currents diverges from that in traditional systems, primarily due to differences in inverter control design and inverter voltage values. Moreover, the fault current in LSPPP-connected networks can manifest as resistive, inductive, or capacitive, which contrasts with SG systems, where it is predominantly inductive.

Effect of LSPPP on distance relay

Figure 1 depicts a transmission line interconnecting with the LSPPP. The solar power plant comprises multiple solar photovoltaic units, which are linked to the collector bus through DC-DC and DC-AC inverters. In the network illustrated in Figure 1.

The Z_{app} observed from bus M is presented in Equation 1 encompasses distinct variables for various types of faults, which are further explored in section “Simulation results”.

$$Z_{app} = \frac{V_{rM}}{I_{rM}} = xZ_{1L} + \left(\frac{I_f}{I_{rM}} \right) R_f = Z_{MF} + \Delta Z \quad [1]$$

This value is calculated by summing the impedance values of the line from bus M to the faulted point, along with a variable impedance ΔZ that depends on network-specific variables. As depicted in Equation (1), the magnitude of ΔZ is contingent upon the ratio of I_f/I_{rM} and the fault resistance. Conversely, one of the distinctive attributes of converters employed in LSPPP is their capability to limit fault current. The limitation of fault current by the LSPPP interfacing converters causes the

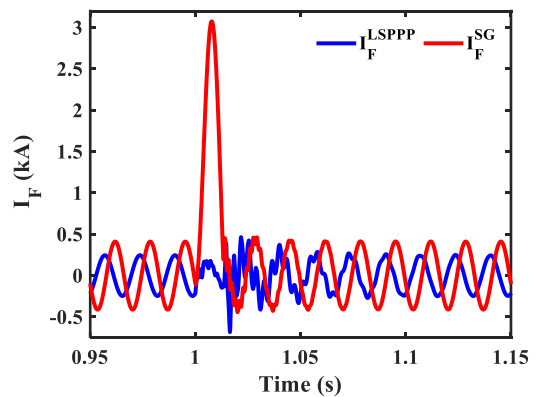


Figure 2. The LSPPP and SG fault currents for a given unbalanced fault

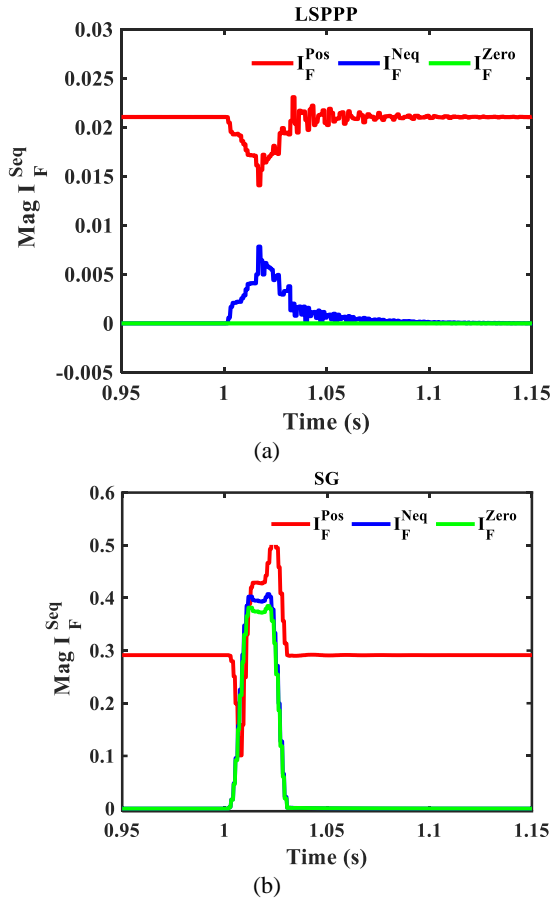


Figure 3. Zero, Negative and Positive fault sequence quantities for (a) LSPPP and (b) SG

ratio I_F/I_{rM} to be significantly higher compared to a conventional power network with synchronous generator-based sources. This alteration leads to a substantial disparity between Z_{MF} and Z_{app} in the presence of LSPPP. The control scheme employed in LSPPP is of paramount importance in determining both the reduction of fault current and the phase angle value. The phase difference between (I_F) and (I_{rM}) is contingent upon the phase angle of the fault current, and as this phase angle undergoes variations, the disparity between them significantly increases. Consequently, these variations result in the introduction of an additional reactance to ΔZ . This added reactance shifts the apparent impedance along the imaginary axis within the R-X plane.

Proposed method

Figure 4(a) illustrates the challenge associated with grid protection in the presence of LSPPP, as elaborated upon in the preceding section. When a fault event transpires, the European Union GC mandates the LSPPP to generate reactive current. This reactive current is injected into the grid-connected bus to uphold the voltage level, this causes, (I_F) leads (I_{rM}) . Figure 4(b) presents the

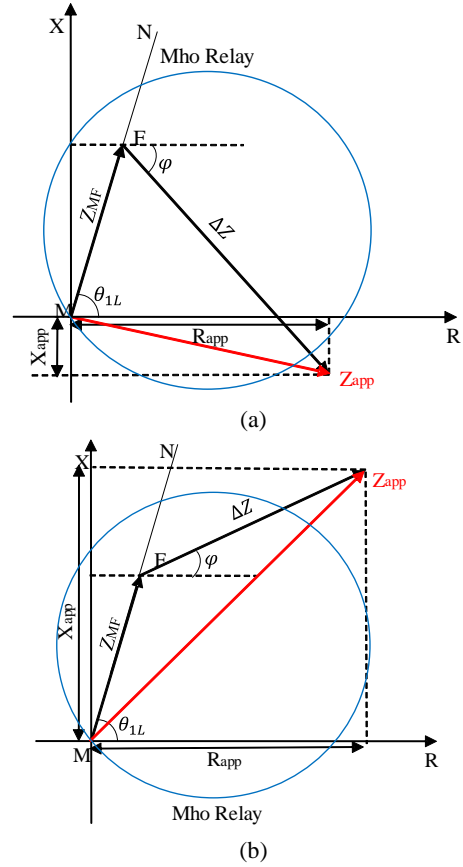


Figure 4. Impedance seen by distance relay, (a) leading and (b) lagging

measured apparent impedance value under these circumstances (30).

The correct operation of the protection system relies on the settings determined by the value of Z_{MF} as indicated in Equation 1. However, based on this relationship, the impedance value measured by the distance relay is derived from the sum of Z_{MF} and ΔZ . Given that the value of Z_{app} is known, Z_{MF} can be calculated by computing ΔZ . The angle φ and Z_{MF} , as depicted in Figure 4, can be determined using geometric properties as shown in Equations 2 and 3 (30).

$$\varphi = \tan^{-1} \left(\frac{|Z_{MF}| \sin \theta_{1L} - X_{app}}{|Z_{MF}| \cos \theta_{1L} - R_{app}} \right) \quad [2]$$

$$Z_{MF} = \frac{X_{app} - R_{app} \tan \varphi}{\sin \theta_{1L} - \cos \theta_{1L} \tan \varphi} (\cos \theta_{1L} + j \sin \theta_{1L}) \quad [3]$$

$$x = \frac{Z_{MF}}{Z_{1L}} \quad [4]$$

Using Equation 4, it is possible to identify the fault location. As depicted in Figure 4, the angle φ represents

the gradient of ΔZ , and its value can be calculated using Equation 5.

$$\varphi = \arg\left(\frac{I_F}{I_{rM}} R_F\right) = \arg\left(\frac{I_F}{I_{rM}}\right) \quad [5]$$

To determine Z_{MF} using Equation 3, it's necessary to calculate φ first, and interface Equation 5 can facilitate this calculation. The angle φ is a function of I_F , as demonstrated in Equation 5. Consequently, it can be concluded that φ is dependent on the current at the remote end. Below is the computation of φ for all types of faults. Additionally, Figure 5 illustrates the discussed sequence networks for all types of faults.

Calculating the phase angle φ

In accordance with Equation 1, which represents the calculated apparent impedance value, expanding the variables along with their complex forms allows us to rewrite it as shown in Equation 6.

$$\frac{|V_{rM}^f|}{|I_{rM}^f|} e^{j(\alpha-\beta)} = x |Z_{1L}| e^{j\theta_{1L}} + \frac{|I_F|}{|I_{rM}^f|} e^{j(\gamma-\beta)} R_F \quad [6]$$

According to Equation 6, Equation 7 is deduced.

$$\arg\left(\frac{|I_F|}{|I_{rM}^f|}\right) = \arg\left(\frac{|V_{rM}^f|}{|I_{rM}^f|} e^{j(\alpha-\gamma)}\right) - \arg\left(|Z_{1L}| e^{j(\theta_{1L}-\gamma+\beta)}\right) \quad [7]$$

The computation of α , β and γ is the next step. It is essential to note that these values vary depending on the specific fault type, necessitating distinct calculations for each fault category to ensure accuracy.

For AG fault

Referring to Figure 5(a) and applying KVL Equation 8 is derived.

$$V_{AM}^f - xZ_{1L}(I_{AM}^f + K_0 I_{0M}^f) - 3R_F I_{0F} = 0 \quad [8]$$

$$K_{0L} = \frac{Z_{0L} - Z_{1L}}{Z_{1L}} \quad [9]$$

Based on Equation 9, the apparent impedance value can be determined as follows:

$$\frac{V_{AM}^f}{(I_{AM}^f + K_0 I_{0M}^f)} = xZ_{1L} + \frac{3I_{0F}}{(I_{AM}^f + K_0 I_{0M}^f)} R_F \quad [10]$$

Through a comparison of Equations 1 and 10:

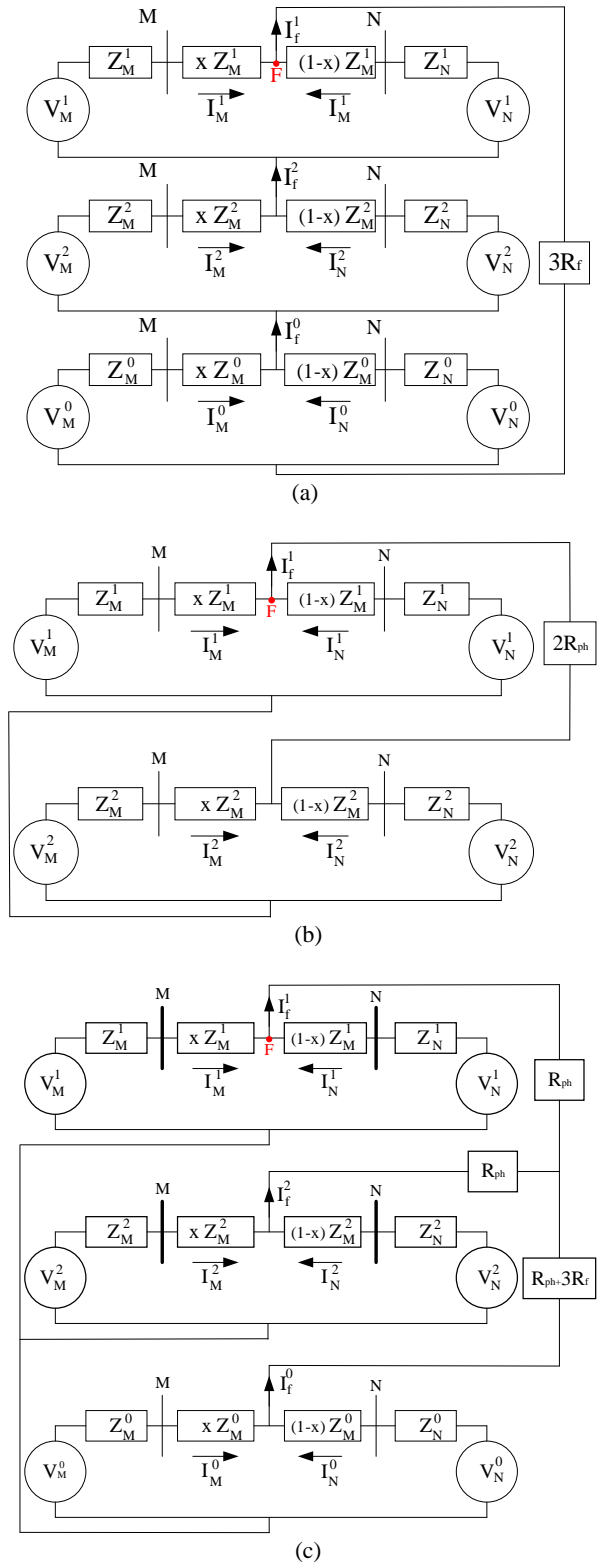


Figure 5. Sequence networks of the system in Figure 1 for (a) AG, (b) BC and (c) BCG faults

$$V_{rM}^f = V_{AM}^f, I_{rM}^f = (I_{AM}^f + K_0 I_{0M}^f), I_F = 3I_{0F} \quad [11]$$

Referring to Equation 8, the necessary phase angles are acquired as follows:

$$\begin{aligned} \alpha &= \arg(V_{AM}^f), \\ \beta &= \arg((I_{AM}^f + K_0 I_{0M}^f)), \\ \gamma &= \arg(3I_{0F}) \end{aligned} \quad [12]$$

Given that the presence of LSPPP eliminates the value of zero-sequence current, γ can be calculated utilizing the local zero-sequence current as per Equation 8.

$$\gamma = \arg(3I_{0F}) = \arg(I_{0M}^f) \quad [13]$$

For BC fault

Referring to Figure 5b and applying KVL, Equation 14 is derived.

$$(V_{1M}^f - V_{2M}^f) - xZ_{1L}(I_{1M}^f - I_{2M}^f) + 2R_{ph}I_{2F} = 0 \quad [14]$$

Based on Equation 14, the apparent impedance value can be determined as follows:

$$\frac{(V_{1M}^f - V_{2M}^f)}{(I_{1M}^f - I_{2M}^f)} = xZ_{1L} - \frac{2I_{2F}}{(I_{1M}^f - I_{2M}^f)}R_{ph} \quad [15]$$

By comparing Equation 1 with Equation 15:

$$V_{rM}^f = (V_{1M}^f - V_{2M}^f), I_{rM}^f = (I_{1M}^f - I_{2M}^f), I_F = -2I_{2F} \quad [16]$$

Based on Equation 9, the necessary phase angles are determined as follows:

$$\begin{aligned} \alpha &= \arg(V_{1M}^f - V_{2M}^f), \\ \beta &= \arg(I_{1M}^f - I_{2M}^f), \\ \gamma &= \arg(-2I_{2F}) \end{aligned} \quad [17]$$

Because LSPPP diminishes the negative sequence current and emulates an apparent sequence reactance, the current remains uniform (35). Consequently, γ in Equation 17 can be computed as shown in Equation 18.

$$\gamma = \arg(-2I_{2F}) = \arg(I_{2M}^f) - \pi \quad [18]$$

Given that in this paper, bus M is exclusively connected to LSPPP, the current I_{2F} does not flow through this bus. Consequently, the current passing through bus N is equal to I_{2M} . In this scenario, V_{2F} is also equal to V_{2M} .

$$I_{2F} = -\frac{V_{2F}^f}{(1-x)Z_{2L}} \quad [19]$$

Therefore, the value of γ can be obtained:

$$\gamma = \arg(-2I_{2F}) = \arg\left(\frac{V_{2M}^f}{Z_{2L}}\right) \quad [20]$$

For BCG fault

Referring to Figure 5(c) and applying KVL, Equation 21 is derived.

$$\begin{aligned} (V_{2M}^f - V_{0M}^f) &= xZ_{2L}(I_{2M}^f - K'_{0L}I_{0M}^f) \\ &\quad - I_{0F}((1-m)R_{ph} + 3R_F) \end{aligned} \quad [21]$$

where, $K'_{0L} = \frac{Z_{0L}}{Z_{1L}}$ and $m = \frac{I_{2L}}{I_{0L}}$. Based on Equation 21,

the apparent impedance value can be determined as follows:

$$\begin{aligned} \frac{(V_{2M}^f - V_{0M}^f)}{(I_{2M}^f - K'_{0L}I_{0M}^f)} &= \\ xZ_{1L} - \frac{I_{0F}}{(I_{2M}^f - K'_{0L}I_{0M}^f)} &((1-m)R_{ph} + 3R_F) \end{aligned} \quad [22]$$

In this equation, R_{ph} is associated with phases. The magnitude of this resistance is considerably smaller in comparison to the fault resistance. Through a comparison of Equations 1 and 22:

$$\begin{aligned} V_{rM}^f &= (V_{2M}^f - V_{0M}^f), \\ I_{rM}^f &= (I_{2M}^f - K'_{0L}I_{0M}^f), \\ I_F &= -I_{0F} \end{aligned} \quad [23]$$

According to Equation 8, the required phase angles are obtained:

$$\begin{aligned} \alpha &= \arg(V_{2M}^f - V_{0M}^f), \\ \beta &= \arg(I_{2M}^f - K'_{0L}I_{0M}^f), \\ \gamma &= \arg(-I_{0F}) = \arg(I_{0M}^f) - \pi \end{aligned} \quad [24]$$

The variable values derived for Equation 1 are elaborated upon in Table 1. Flowchart of the proposed method shows the Figure 6.

Table 1. Calculate the relation of the distance relay for different faults

| Fault type | AG | BC | BCG |
|------------|---------------------------|-----------------------|-------------------------------|
| V_{rM} | V_{AM}^F | $V_{1M}^F - V_{2M}^F$ | $V_{2M}^F - V_{0M}^F$ |
| I_{rM} | $I_{AM}^F + K_0 I_{0M}^F$ | $I_{1M}^F - I_{2M}^F$ | $I_{2M}^F - K'_{0L} I_{0M}^F$ |
| I_F | I_{0M}^F | $-2I_{2F}$ | $-I_{0F}$ |

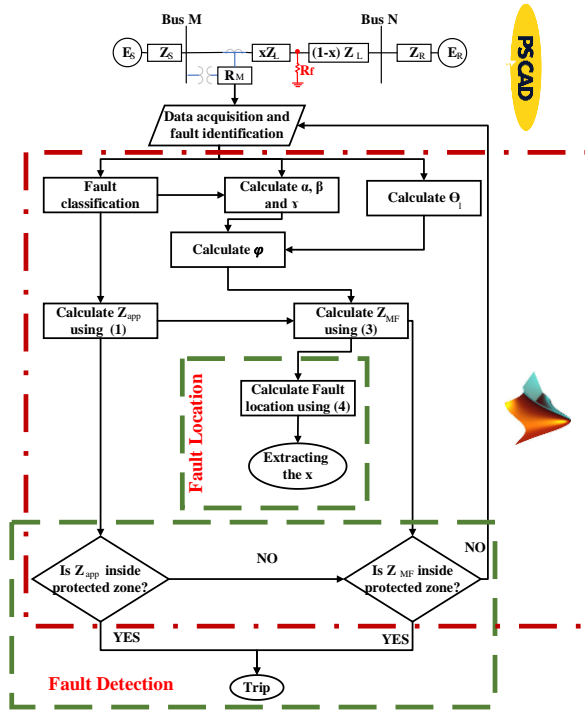


Figure 6. Flowchart of the proposed algorithm

SIMULATION RESULTS

Figure 1 illustrates the simulated system, which consists of a 230 kV, 60 Hz power source on one side and a 100 MW PV plant with a double-stage connection to bus M through a dYg1 transformer, is employed to optimize the PV plant's power output using Maximum Power Point Tracking (MPPT) (37) in the boost converter. Specific details regarding the PV plant and the M-N line can be found in Table 2 (38). Voltage and current signals are collected at relay R_M 's location (bus M) with a sampling frequency of 2 kHz. To evaluate the method's performance, various scenarios were simulated. The source impedance connected to bus N is $9.186 + j0.138 \Omega$.

Figure 7 illustrates the impedance measured by the distance relay in the presence of LSPPP compared to the traditional system. As depicted in the figure, the presence of LSPPP alters the measured impedance, increasing the likelihood of a malfunction in the protection system.

Figure 8 illustrates the impedance measured by the distance relay using the proposed algorithm under the same conditions as Figure 7. It is evident that the performance is acceptable and closely aligns with the desired value.

Effects of faults at different locations

Figure 9 displays the impedance measured by the distance relay using the proposed algorithm for various fault locations. In this figure, fault location is relative to the

Table 2. Sample system data

| Component | Specifications |
|----------------------|---|
| LSPPP | Number of PV arrays & cells in series per module: 130, 35, irradiance: $1000 \text{ W} / \text{m}^2$, $K_p = 0.15$ & $T_i = 0.08 \text{ s}$, DC Link capacitor: $7800 \mu\text{F}$, $L_f = 300 \mu\text{H}$, $C_f = 200 \mu\text{F}$, $R_f = 0.025 \Omega$. |
| Line M-N Parameters: | $Z_L^1 = Z_L^2 = 0.03293 + j 0.327 \Omega / \text{km}$, $Z_L^0 = 0.2587 + j 1.1740 \Omega / \text{km}$, $C_1 = 280.1 \text{ M}\Omega / \text{km}$, $C_0 = 461.2546 \text{ M}\Omega / \text{km}$, $L = 100 \text{ km}$ |

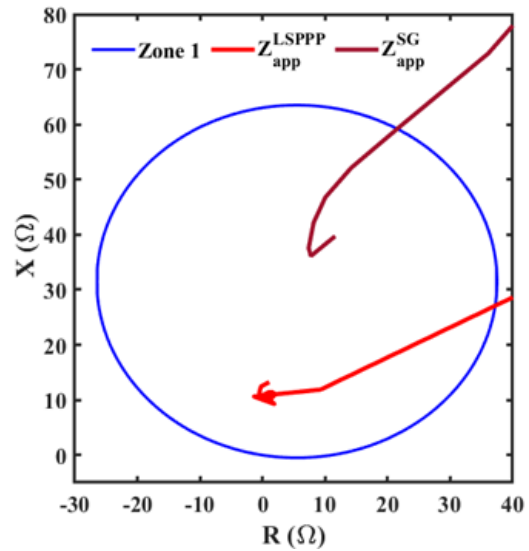


Figure 7. Performance of distance relay for LSPPP and SG

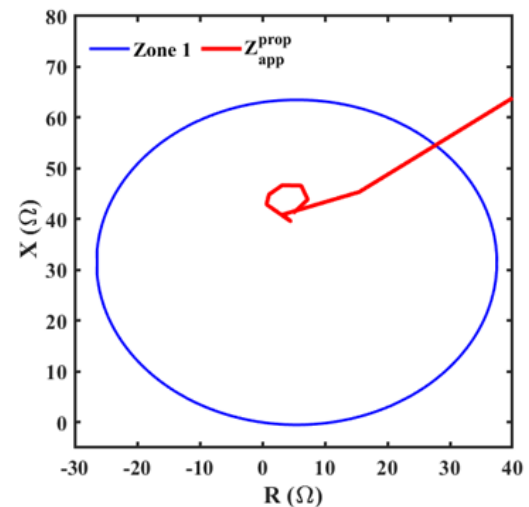


Figure 8. the measured impedance by distance relay with proposed algorithm

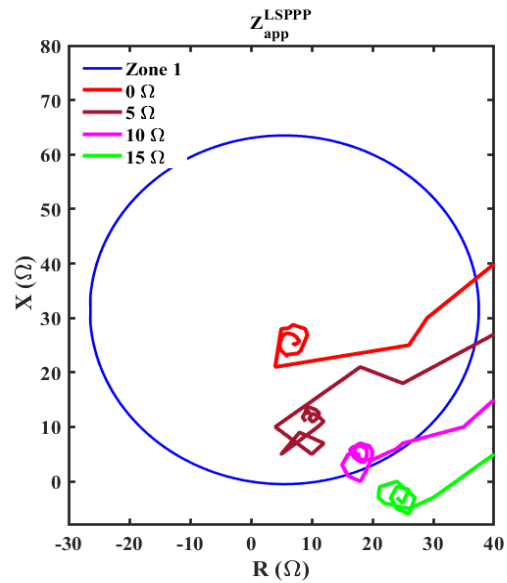
relay's position, and a fault resistance of 10Ω is assumed. Table 3 presents simulation results for different faults categorized by their respective locations. The presented algorithm's effectiveness is demonstrated in this table through the application of the Euclidean distance (D_{EUC}) principle. Table 3 reveals that, under various homogeneity conditions, the Euclidean distance remains consistently below 2.

Table 3. The results of applying the proposed algorithm for fault at different locations and comparing its results with the results before applying the algorithm and the results of the SG network

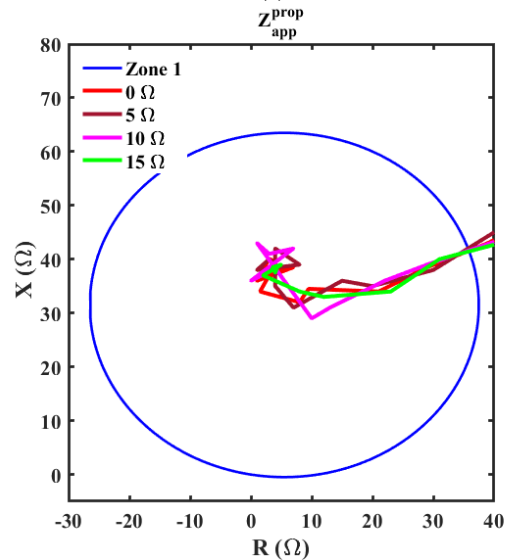
| Fault type | X (Km) | D_{EUC}^{SG} | D_{EUC}^{LSPPP} | D_{EUC}^{prop} | X^{prop} (km) |
|------------|--------|----------------|-------------------|------------------|-----------------|
| AG | 10 | 12.8 | 18.03 | 0.92 | 10.4 |
| | 30 | 13.4 | 20.42 | 1.12 | 29.7 |
| | 50 | 16.38 | 21.93 | 1.55 | 50.6 |
| | 70 | 20.5 | 46.1 | 1.81 | 70.9 |
| BC | 10 | 20.3 | 7.5 | 0.31 | 10.3 |
| | 30 | 21.3 | 11.2 | 0.98 | 30.5 |
| | 50 | 23.5 | 20.6 | 1.31 | 50.6 |
| | 70 | 29.4 | 35.2 | 1.69 | 68.9 |
| BCG | 10 | 15.7 | 12.3 | 0.87 | 10.5 |
| | 30 | 22.3 | 18.4 | 1.2 | 30.4 |
| | 50 | 26.9 | 25.4 | 1.43 | 49.3 |
| | 70 | 31.2 | 36.7 | 1.78 | 70.9 |

Effects of different fault resistances

As indicated in Equation 1, the rise in fault resistance directly leads to an increase in the apparent impedance observed by the distance relay. Furthermore, as previously noted, the presence of LSPPP reduces the fault current magnitude, and concurrently, the control operation of the power plant alters the current angles at both ends. Consequently, the impact of fault resistance is considerably more pronounced compared to traditional systems. Consequently, an increase in this value results in a substantial deviation from the actual impedance value.



(a)



(b)

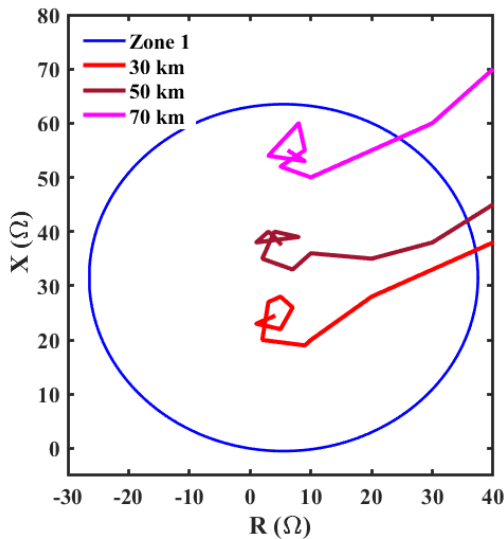


Figure 9. measured impedance by distance relay with the proposed algorithm for different fault locations

Figure 10. Demonstrating the influence of R_f

The extent of this variation is contingent upon the current angle between the two ends of the transmission line. The outcomes, demonstrating the impact of R_f , can be observed in Figure 10. Additionally, simulation results for various fault types with varying fault resistances are provided in Table 4. This table offers a comparison of results between three scenarios: the traditional system, the system with LSPPP, and the system with LSPPP implemented with the proposed algorithm. It's important to note that x is set to 50 Km in this analysis.

Effects of variable LSPPP generation

Taking into consideration that fluctuations in the power generation of renewable power plants can impact pre-fault voltage and current, resulting in modifications to the equivalent impedance of the plant, there is an increased risk of distance relay maloperation. Figure 11(a) illustrates the impedance value observed by the distance relay in the presence of LSPPP at various power generation levels for this power plant. Figure 11(b) presents the measured impedance value based on the proposed algorithm. This case is specifically examined for AG fault with $R_f = 5 \Omega$, $x = 50$ Km. This figure demonstrates that the proposed method for calculating the impedance observed by the distance relay remains unaffected by LSPPP generation.

The influence of noise

The method described in this study effectively minimizes the influence of noise in the recorded signals. To assess the impact of noise on the recorded signals, white noise with a spectral power density of 10% was intentionally added. The algorithm's performance was then evaluated through a series of simulation experiments, covering various fault types, fault location, and fault resistances.

Table 4. The results of proposed algorithm for variable fault resistance and comparing its results with the results before applying the algorithm and the results of the SG network

| Fault type | R_f (Ω) | D_{EUC}^{SG} | D_{EUC}^{LSPPP} | D_{EUC}^{prop} | prop (km) |
|------------|--------------------|----------------|-------------------|------------------|-----------|
| AG | 0 | 11.3 | 18.4 | 0.9 | 50.3 |
| | 10 | 16.38 | 21.93 | 1.55 | 50.6 |
| | 100 | 30.9 | 36.5 | 1.86 | 49.1 |
| | 150 | 46.8 | 45.2 | 2.02 | 51.3 |
| BC | 0 | 18.5 | 14.2 | 0.87 | 50.2 |
| | 10 | 23.5 | 20.6 | 1.31 | 50.6 |
| | 100 | 49.4 | 40.2 | 1.62 | 50.8 |
| BCG | 0 | 22.7 | 19.7 | 1.03 | 50.4 |
| | 10 | 26.9 | 25.4 | 1.43 | 49.3 |
| | 100 | 53.8 | 38.2 | 1.82 | 51 |
| | 150 | 69.4 | 49.8 | 2.1 | 51.4 |

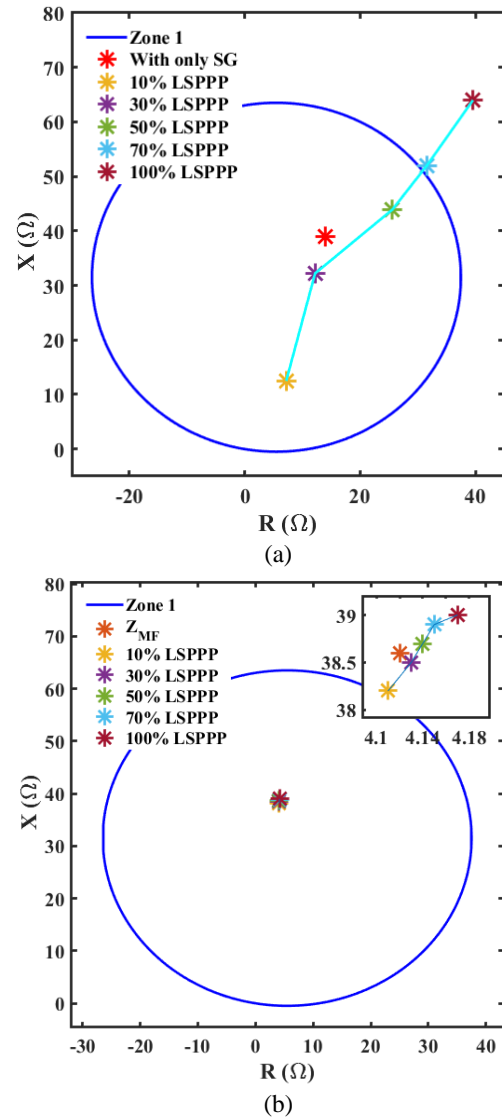


Figure 11. demonstrating the influence of change in renewable plant generation (a) Conventional method, (b) Proposed method

The simulation results are presented in Table 5. A comparison between two cases, one with noise in the measured signals and one without, reveals that the presence of noise in the signals did not significantly impact the accuracy of fault detection.

Performance in the IEEE 39-Bus test system

The IEEE 39-bus standard test system has been employed as a reference for constructing a simulated power transmission system. In order to generate fault samples, a robust transient simulation environment is required, and for this purpose, PSCAD/EMTDC has been chosen as the simulation software. As depicted in Figure 12, the electrical single-line diagram of the 39-bus system is illustrated. The IEEE 39-bus standard test system

comprises 10 generators, 12 three-phase transformers, 34 transmission lines, and several loads. This larger system has been employed for the evaluation and validation of the proposed algorithm's performance (39). The generator connected at bus 33 is replaced by a 100 MW LSPPP. To assess the algorithm's performance under various fault scenarios on line 19-16, simulations were conducted with different fault types, fault locations, and fault resistances. The results of these simulations are presented in Table 6. This table shows the results of different types of faults in two different fault locations and three values of fault resistance for the IEEE 39-bus standard test system. In addition to comparing the results of Euclidean distance index of the proposed method with the results of the system with SG and the system connected to LSPPP with traditional protection, this table also shows the effect of noise. As can be seen, the effect of fault resistance, fault location, fault type and noise on the performance of the proposed method is very insignificant and the proposed method has been successful in calculating the actual impedance value seen by the distance relay. Other information that can be seen from this table is the results related to the estimation of the fault location. As it can be seen, the proposed method has a successful performance in detecting the fault location for the mentioned scenarios,

and the effect of noise has had a negligible effect on this detection.

Advantages of the proposed algorithm and comparative assessment

Over the past few years, several articles have investigated the performance of the distance relay under similar conditions to those outlined in this article. In this section, the method proposed in this article is compared with that of previous articles. The outcomes of this comparison are presented in Table 7. These articles have investigated low fault resistance and the performance of their methods against high resistance faults is not clear. The presented methods by Chao et al. (35) have used quadrilateral characteristic. Also, in the quadrilateral characteristic, to prevent the increase of the characteristic area, the maximum setting value of fault resistance cannot be considered more than a specific value. The proposed method by Liang et al. (40) is only for asymmetrical faults. In these papers, a sampling frequency value is not mentioned or a high value is considered, which will increase the number of calculations. Another important factor that must be investigated in power systems is the impact of noise, which is not discussed in these articles.

Table 5. The influence of noisy conditions on the performance of the proposed protection scheme

| Fault type | X (km) | R_f (Ω) | Without noise in measured signals | | With noise in measured signals | | |
|------------|--------|--------------------|-----------------------------------|-----------------|--------------------------------|-----------------|------|
| | | | D_{EUC}^{prop} | X^{prop} (km) | D_{EUC}^{prop} | X^{prop} (km) | |
| AG | 0.3 | 10 | 1.12 | 29.7 | 1.23 | 30.4 | |
| | | 100 | 1.75 | 30.4 | 1.78 | 30.8 | |
| | | 150 | 1.89 | 30.8 | 1.96 | 29.1 | |
| | 0.7 | 10 | 1.81 | 70.9 | 1.84 | 69.2 | |
| | | 100 | 1.92 | 71.03 | 1.99 | 71.5 | |
| | | 150 | 2.01 | 71.2 | 2.11 | 68.2 | |
| | BC | 0.3 | 10 | 0.98 | 30.5 | 1.31 | 30.9 |
| | | | 100 | 1.51 | 29.1 | 1.63 | 31.4 |
| | | | 150 | 1.79 | 31.2 | 1.86 | 32.1 |
| 0.7 | | 10 | 1.69 | 68.9 | 1.98 | 70.2 | |
| | | 100 | 1.73 | 70.9 | 2.04 | 71.3 | |
| | | 150 | 2.03 | 71.2 | 2.16 | 68.7 | |
| BCG | 0.3 | 10 | 1.2 | 30.4 | 1.34 | 30.6 | |
| | | 100 | 1.49 | 30.9 | 1.58 | 31.5 | |
| | | 150 | 1.76 | 29.1 | 1.87 | 32.4 | |
| | 0.7 | 10 | 1.78 | 70.9 | 1.93 | 70.7 | |
| | | 100 | 1.89 | 71.3 | 2.07 | 72.3 | |
| | | 150 | 2.02 | 68.7 | 2.12 | 73.1 | |

Table 6. Evaluation of the proposed scheme in the IEEE 39-Bus system

| Fault type | X (p.u) | R _f (Ω) | D _{EUC} ^{SG} | D _{EUC} ^{LSPPP} | Without noise in measured signals | | With noise in measured signals | |
|------------|---------|--------------------|--------------------------------|-----------------------------------|-----------------------------------|-------------------------|----------------------------------|-------------------------|
| | | | | | D _{EUC} ^{prop} | X ^{prop} (p.u) | D _{EUC} ^{prop} | X ^{prop} (p.u) |
| AG | 0.3 | 10 | 11.3 | 17.2 | 0.84 | 0.309 | 0.86 | 0.318 |
| | | 100 | 24.5 | 29.8 | 1.6 | 0.311 | 1.6 | 0.331 |
| | | 150 | 33.7 | 51.2 | 1.97 | 0.287 | 2 | 0.392 |
| | 0.7 | 10 | 14.8 | 19.1 | 0.95 | 0.704 | 0.98 | 0.697 |
| | | 100 | 26.8 | 36.1 | 1.74 | 0.691 | 1.82 | 0.734 |
| | | 150 | 44.3 | 59.4 | 1.88 | 0.714 | 1.93 | 0.781 |
| BC | 0.3 | 10 | 8.9 | 14.2 | 0.94 | 0.305 | 0.98 | 0.324 |
| | | 100 | 19.4 | 27.1 | 1.44 | 0.296 | 1.56 | 0.361 |
| | | 150 | 37.8 | 55.3 | 1.84 | 0.291 | 1.98 | 0.284 |
| | 0.7 | 10 | 15.6 | 19.7 | 1.1 | 0.709 | 1.3 | 0.714 |
| | | 100 | 28.2 | 35.4 | 1.67 | 0.713 | 1.72 | 0.733 |
| | | 150 | 46.2 | 61.2 | 2.04 | 0.723 | 2.1 | 0.692 |
| BCG | 0.3 | 10 | 10.3 | 16.5 | 0.92 | 0.302 | 1.1 | 0.305 |
| | | 100 | 29.8 | 33.2 | 1.54 | 0.309 | 1.69 | 0.315 |
| | | 150 | 38.7 | 44.3 | 1.84 | 0.314 | 2.02 | 0.331 |
| | 0.7 | 10 | 14.9 | 18.4 | 1.02 | 0.697 | 1.3 | 0.702 |
| | | 100 | 38.2 | 41.3 | 1.57 | 0.691 | 1.8 | 0.714 |
| | | 150 | 47.3 | 63.7 | 1.79 | 0.722 | 2.1 | 0.743 |

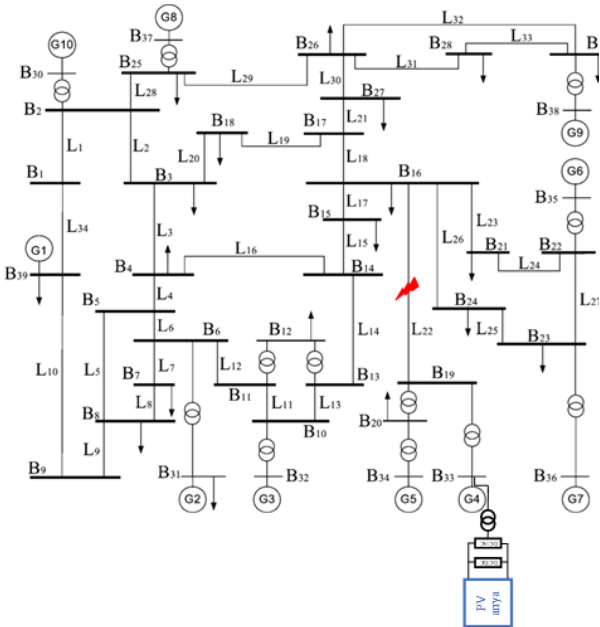


Figure 12. LSPPP integrated IEEE 39-bus standard test system

Table 7. Papers Comparison

| Parameters | References | | | | Proposed method |
|-------------------------------------|------------|------|------|------|-----------------|
| | (36) | (40) | (27) | (35) | |
| Applicable for all types of faults? | Yes | No | Yes | No | Yes |
| Variable generation | No | No | Yes | Yes | Yes |
| Independent on pre-fault data | Yes | No | No | No | Yes |
| High resistance fault detection | No | No | No | Yes | Yes |
| Sampling frequency (kHz) | N-M* | N-M | 3.84 | N-M | 2 |
| Calculate the fault location | No | No | No | No | Yes |
| Performance in noise condition | No | No | No | No | Yes |

*N-M= Not Mentioned

CONCLUSION

The existence of LSPPP within the network results in the modulation of fault characteristics. Additionally, the operation of converter control introduces another factor that alters these fault characteristics. As a consequence of these changes, the conventional distance relay algorithm may malfunction, particularly in scenarios involving faults with high fault resistance. Investigating the vulnerability and identifying the factors affecting the performance of the distance relay in zone 1 is mandatory in such conditions. In this article, this vulnerability and effective factors are investigated and a new method is proposed to improve the performance and estimate the fault location. The suggested approach relies on the estimation of the faulted path current angle. In this methodology, local voltage and current data are employed to ascertain the phase angle value of the fault loop current. Following the determination of the phase angle value, the impedance of the transmission line up to the fault location is computed. The distance relay then utilizes this impedance value to make a decision. This algorithm has been thoroughly examined for various fault types, encompassing different resistance values, diverse fault locations, varying LSPPP generation levels, and noise condition.

The proposed scheme offers several key advantages and innovations, including the following:

- The proposed method demonstrated satisfactory performance at a sampling frequency of 2 kHz, resulting in reduced computational complexity and faster fault detection compared to other studies that either overlooked this aspect or examined it with a higher sampling frequency.
- In this paper, the effectiveness of the proposed algorithm is demonstrated using the application of the Euclidean distance, and the value of this distance is compared for three scenarios: SG based systems, traditional methods in the presence of LSPPP, and the proposed method. The utilization of the Euclidean distance aids in better understanding the impact of LSPPP on the measured impedance and it also shows the excellent performance of the proposed algorithm.
- This algorithm, in addition to its excellent fault detection capability, also possesses the ability to the fault location.
- This algorithm possesses the capability of identifying with a higher level of fault resistance compared to other studies. Furthermore, it is capable of identifying various types of faults.

The results obtained from these investigations are compared with those of the conventional method to demonstrate the benefits and advantages of the proposed approach. For future studies, we can suggest things such as further reduction of sampling frequency, identification

of faults with higher resistance and identification of single-phase faults with non-linear characteristics.

REFERENCES

1. Salazar-Chiralt R, Cheah-Mane M, Mateu-Barriendos E, Bullich-Massague E, Prieto-Araujo E, Mehrjerdi H, Gomis-Bellmunt O. Dynamic interactions in large scale photovoltaic power plants with frequency and voltage support. *Electric Power Systems Research*. 2022; 207: 107848. Doi: 10.1016/j.epsr.2022.107848
2. Pishkar I, M Beigi S. A comprehensive evaluation of renewable energy systems with a backup to provide a part of electrical needs of a hospital: A case study in grid-connected mode. *Iranica Journal of Energy & Environment*. 2024; 15(1): 1-9. Doi: 10.5829/IJEE.2024.15.01.01
3. Vrana TK, Attya A, Trilla L. Future-oriented generic grid code regarding wind power plants in Europe. *International Journal of Electrical Power & Energy Systems*. 2021; 125: 106490. Doi: 10.1016/j.ijepes.2020.106490
4. Tahiru A-W, Takal S, Sunkari E, Ampofo S. A Review on renewable energy scenario in Ethiopia. *Iranian (Iranica) Journal of Energy & Environment*. 2023; 14(4): 372-84. Doi: 10.5829/ijee.2023.14.04.07
5. Varma RK, Akbari M. Simultaneous fast frequency control and power oscillation damping by utilizing PV solar system as PV-STATCOM. *IEEE Transactions on Sustainable Energy*. 2019; 11(1): 415-25. Doi: 10.1109/TSTE.2019.2892943
6. Ryu A, Ishii H, Hayashi Y. Battery smoothing control for photovoltaic system using short-term forecast with total sky images. *Electric Power Systems Research*. 2021; 190: 106645. Doi: 10.1016/j.epsr.2020.106645
7. Hasanien HM. An adaptive control strategy for low voltage ride through capability enhancement of grid-connected photovoltaic power plants. *IEEE Transactions on power systems*. 2015; 31(4): 3230-7. Doi: 10.1109/TPWRS.2015.2466618
8. Haddadi A, Farantatos E, Kocar I, Karaagac U. Impact of inverter based resources on system protection. *Energies*. 2021; 14(4): 1050. Doi: 10.3390/en14041050
9. Kou G, Chen L, VanSant P, Velez-Cedeno F, Liu Y. Fault characteristics of distributed solar generation. *IEEE Transactions on Power Delivery*. 2019; 35(2): 1062-4. Doi: 10.1109/TPWRD.2019.2907462
10. Kauffmann T, Karaagac U, Kocar I, Jensen S, Mahseredjian J, Farantatos E. An accurate type III wind turbine generator short circuit model for protection applications. *IEEE Transactions on Power Delivery*. 2016; 32(6): 2370-9. Doi: 10.1109/TPWRD.2016.2614620
11. Kauffmann T, Karaagac U, Kocar I, Jensen S, Farantatos E, Haddadi A, Mahseredjian J. Short-circuit model for type-IV wind turbine generators with decoupled sequence control. *IEEE Transactions on Power Delivery*. 2019; 34(5): 1998-2007. Doi: 10.1109/TPWRD.2019.2908686
12. Kauffmann T, Karaagac U, Kocar I, Gras H, Mahseredjian J, Cetindag B, Farantatos E. Phasor domain modeling of type III wind turbine generator for protection studies. 2015 IEEE Power & Energy Society General Meeting. 2015: 1-5. Doi: 10.1109/PESGM.2015.7286606
13. Nagpal M, Jensen M, Higginson M. Protection challenges and practices for interconnecting inverter based resources to utility transmission systems. *IEEE Power Energy Soc*. 2020: 1-65. Doi: 10.13140/RG.2.2.22715.90406
14. Hooshyar A, Azzouz MA, El-Saadany EF. Distance protection of lines connected to induction generator-based wind farms during balanced faults. *IEEE Transactions on Sustainable Energy*. 2014; 5(4): 1193-203. Doi: 10.1109/TSTE.2014.2336773

15. Hooshyar A, Azzouz MA, El-Saadany EF. Distance protection of lines emanating from full-scale converter-interfaced renewable energy power plants—Part I: Problem statement. *IEEE Transactions on Power Delivery*. 2014; 30(4): 1770-80. Doi: 10.1109/TPWRD.2014.2369479
16. Hooshyar A, Azzouz MA, El-Saadany EF. Distance protection of lines emanating from full-scale converter-interfaced renewable energy power plants—Part II: Solution description and evaluation. *IEEE Transactions on Power Delivery*. 2014; 30(4): 1781-91. Doi: 10.1109/TPWRD.2014.2369480
17. Haddadi A, Kocar I, Farantatos E. Impact of inverter-based resources on protection schemes based on negative sequence components. EPRI: Palo Alto, CA, USA. 2019; 36(1): 289-98. Doi: 10.1109/TPWRD.2020.2978075
18. Guttromson R. Impact of inverter based resource (IBR) negative sequence current injection on transmission system protection. 2020. Available at: <https://www.osti.gov/servlets/purl/1810044>
19. Kou G, Jordan J, Cockerham B, Patterson R, VanSant P. Negative-sequence current injection of transmission solar farms. *IEEE Transactions on Power Delivery*. 2020; 35(6): 2740-3. Doi: 10.1109/TPWRD.2020.3014783
20. Haddadi A, Kocar I, Karaagac U, Mahseredjian J, Farantatos E. Impact of renewables on system protection: wind/PV short-circuit phasor model library and guidelines for system protection studies. EPRI, USA. 2017. Available at: <https://www.epri.com/research/products/3002002810>
21. Haddadi A, Kocar I, Mahseredjian J, Karaagac U, Farantatos E. Negative sequence quantities-based protection under inverter-based resources Challenges and impact of the German grid code. *Electric Power Systems Research*. 2020; 188: 106573. Doi: 10.1016/j.epsr.2020.106573
22. Haddadi A, Kocar I, Karaagac U, Gras H, Farantatos E. Impact of wind generation on power swing protection. *IEEE Transactions on Power Delivery*. 2019; 34(3): 1118-28. Doi: 10.1109/TPWRD.2019.2896135
23. Singh B, Kumar S, Jain C. Damped-SOGI-based control algorithm for solar PV power generating system. *IEEE Transactions on Industry Applications*. 2017; 53(3): 1780-8. Doi: 10.1109/TIA.2017.2677358
24. Rosini A, Mestriner D, Labella A, Bonfiglio A, Procopio R. A decentralized approach for frequency and voltage regulation in islanded PV-Storage microgrids. *Electric Power Systems Research*. 2021; 193: 106974. Doi: 10.1016/j.epsr.2020.106974
25. Crăciun B-I, Kerekes T, Séra D, Teodorescu R. Frequency support functions in large PV power plants with active power reserves. *IEEE Journal of Emerging and Selected Topics in Power Electronics*. 2014; 2(4): 849-58. Doi: 10.1109/JESTPE.2014.2344176
26. Al Awadhi N, El Moursi MS. A novel centralized PV power plant controller for reducing the voltage unbalance factor at transmission level interconnection. *IEEE Transactions on Energy Conversion*. 2016; 32(1): 233-43. Doi: 10.1109/TEC.2016.2620477
27. Paladhi S, Pradhan AK. Adaptive distance protection for lines connecting converter-interfaced renewable plants. *IEEE Journal of Emerging and Selected Topics in Power Electronics*. 2020; 9(6): 7088-98. Doi: 10.1109/JESTPE.2020.3000276
28. Armendariz M, Paridari K, Wallin E, Nordström L. Comparative study of optimal controller placement considering uncertainty in PV growth and distribution grid expansion. *Electric Power Systems Research*. 2018; 155: 48-57. Doi: 10.1016/j.epsr.2017.10.001
29. Liang Y, Lu Z, Li W, Zha W, Huo Y. A novel fault impedance calculation method for distance protection against fault resistance. *IEEE Transactions on Power Delivery*. 2019; 35(1): 396-407. Doi: 10.1109/TPWRD.2019.2920690
30. Mansouri N, Lashab A, Sera D, Guerrero JM, Cherif A. Large photovoltaic power plants integration: A review of challenges and solutions. *Energies*. 2019; 12(19): 3798. Doi: 10.3390/en12193798
31. Gallo D, Langella R, Testa A, Hernandez J, Papič I, Blažič B, Meyer J. Case studies on large PV plants: Harmonic distortion, unbalance and their effects. 2013 IEEE Power & Energy Society General Meeting. 2013: 1-5. Doi: 10.1109/PESMG.2013.6672271
32. Jalilian A, Muttaqi KM, Sutanto D, Robinson D. Distance Protection of Transmission Lines in Presence of Inverter-based Resources: A New Earth Fault Detection Scheme during Asymmetrical Power Swings. *IEEE Transactions on Industry Applications*. 2022; 58(2): 1899-909. Doi: 10.1109/TIA.2022.3146219
33. Paladhi S, Pradhan AK. Adaptive fault type classification for transmission network connecting converter-interfaced renewable plants. *IEEE Systems Journal*. 2020; 15(3): 4025-36. Doi: 10.1109/JSYST.2020.3010343
34. Rajapakse A, Majumder R, Energy SGR, Nelson R. Modification of commercial fault calculation programs for wind turbine generators. *IEEE Power Energy Society (June 2020)*. 2020: 81. Available at: <https://www.pes-psrc.org/kb/report/093.pdf>
35. Chao C, Zheng X, Weng Y, Liu Y, Gao P, Tai N. Adaptive distance protection based on the analytical model of additional impedance for inverter-interfaced renewable power plants during asymmetrical faults. *IEEE Transactions on Power Delivery*. 2021; 37(5): 3823-34. Doi: 10.1109/TPWRD.2021.3138128
36. Fang Y, Jia K, Yang Z, Li Y, Bi T. Impact of inverter-interfaced renewable energy generators on distance protection and an improved scheme. *IEEE Transactions on Industrial Electronics*. 2018; 66(9): 7078-88. Doi: 10.1109/TIE.2018.2873521
37. Jamiati M. Modeling of Maximum Solar Power Tracking by Genetic Algorithm Method. *Iranian (Iranica) Journal of Energy & Environment*. 2021; 12(2): 118-24. Doi: 10.5829/IJEE.2021.12.02.03
38. Chowdhury A, Paladhi S, Pradhan AK. Nonunit protection of parallel lines connecting solar photovoltaic plants. *IEEE Systems Journal*. 2022. Doi: 10.1109/JSYST.2022.3229349
39. Taylo ADC. *IEEE 39 Bus System*. . 2018. Available at: http://psdyn.ece.wisc.edu/IEEE_benchmarks
40. Liang Y, Li W, Huo Y. Zone I distance relaying scheme of lines connected to MMC-HVDC stations during asymmetrical faults: Problems, challenges, and solutions. *IEEE Transactions on Power Delivery*. 2020; 36(5): 2929-41. Doi: 10.1109/TPWRD.2020.3030332

COPYRIGHTS

©2024 The author(s). This is an open access article distributed under the terms of the Creative Commons Attribution (CC BY 4.0), which permits unrestricted use, distribution, and reproduction in any medium, as long as the original authors and source are cited. No permission is required from the authors or the publishers.



Persian Abstract

چکیده

در این مقاله، یک روش جدید برای تشخیص و مکان یابی خطا برای سیستم های قدرت متصل به نیروگاه فتوولتائیک مقیاس بزرگ (LSPPP) پیشنهاد شده است. ویژگی های اتصال کوتاه (SC) در سیستم های فتوولتائیک به طور قابل توجهی با ژنراتورهای سنکرون (SGs) متفاوت است، در نتیجه، انتظار می رود استفاده روزافزون از LSPPP در سیستم قدرت بر عملکرد طراحی های رله حفاظتی سنتی که در اصل برای سیستم های تحت سلطه SG ها طراحی شده بودند، تأثیر بگذارد. بنابراین، روش پیشنهادی مبتنی بر تجزیه و تحلیل اثرات LSPPP در محاسبه امیدانس واقعی خط انتقال دیده شده، توسط رله دیستانس، برای شناسایی خطا و مکان یابی خطا طراحی شده است. علاوه بر این، محاسبه زاویه فاز جریان حلقه خطا با در نظر گرفتن عواملی مانند محل خطا، مقاومت خطا، انواع خطا، مقدار تولید LSPPP و شرایط نوبز در این مقاله در نظر گرفته شده است. این روش با استفاده از سیستم های تست ۲ باس و ۳۹ باس IEEE متصل به یک LSPPP، شبیه سازی شده در نرم افزارهای PSCAD/EMTDC و MATLAB/SIMULINK، آزمایش و ارزیابی شده است.